Accepted Manuscript

Title: Bio-template assisted solvothermal synthesis of broom-like $BaTiO_3$: Nd^{3+} hierarchical architectures for display and forensic applications

Authors: M. Dhanalakshmi, H. Nagabhushana, S.C. Sharma, R.B. Basavaraj, G.P. Darshan, D. Kavyashree

PII: S0025-5408(17)34135-1
DOI: https://doi.org/10.1016/j.materresbull.2018.02.003
Reference: MRB 9827

To appear in: *MRB*

Received date: 3-11-2017
Revised date: 4-1-2018
Accepted date: 1-2-2018

Please cite this article as: Dhanalakshmi M, Nagabhushana H, Sharma SC, Basavaraj RB, Darshan GP, Kavyashree D, Bio-template assisted solvothermal synthesis of broom-like $BaTiO_3$: Nd^{3+} hierarchical architectures for display and forensic applications, *Materials Research Bulletin* (2010), https://doi.org/10.1016/j.materresbull.2018.02.003

Bio-template assisted solvothermal synthesis of broom-like $BaTiO_3:Nd^{3+}$ hierarchical architectures for display and forensic applications

M. Dhanalakshmi[1, 2], H. Nagabhushana[3*], S.C. Sharma[4, 5], R.B. Basavaraj[3], G.P. Darshan[6], D. Kavyashree[7]

[1]Department of Physics, Govt. Science College, Bengaluru-560 001, India
[2]Research and Development Center, Bharathiar University, Coimbatore 641046, India
[3]Prof. C.N.R. Rao Centre for Advanced Materials, Tumakuru University, Tumakuru-572103, India
[4]Advisor, Avinashilingam Institute for Home Science and Higher Education for Women University, Coimbatore 641043, India
[5]Department of Mechanical Engineering, Jain University, Advisor, Jain group of Institutions, Bangalore 560069, India
[6]Department of Physics, Acharya Institute of Graduate Studies, Bangalore 560 107, India
[7]Department of Physics, Channabasaveshwara Institute of Technology, VTU affiliated, Gubbi 572 216, India

* Corresponding authors. +91- 9945954010, E-mail addresses: bhushanvlc@gmail.com (H. Nagabhushana).

Graphical abstract

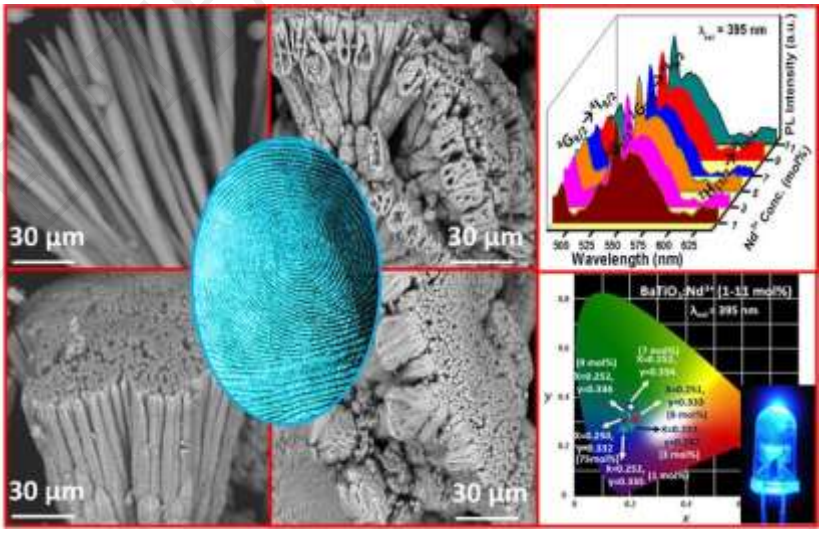

Research highlights

1. Broom-like $BaTiO_3:Nd^{3+}$ structures were prepared by solvothermal route using CTAB surfactant.
2. Morphologies were highly dependent on temperature, pH, surfactant concentration and time durations.
3. LFPs were visualized on various porous and non-porous surfaces.
4. Photometric studies were carried out for display applications.

Abstract

Broom-like hierarchical structures of $BaTiO_3:Nd^{3+}$ (1-11 mol %) nanophosphors (NPs) were fabricated via CTAB assisted solvothermal route. Controlled experiments namely, reaction temperature, surfactant concentration, pH and time duration were performed and its influences on morphology of the product was investigated. These conditions may tune the simple structures to broom-like hierarchical structures. The energy band gap (E_g) of the synthesized NPs were estimated to be ~ 3.29-3.42 eV. Judd–Ofelt (J-O) intensity parameters were calculated by utilizing the PL emission spectra instead of normal absorption spectra. The CIE and CCT results indicate that the NPs exhibit intense blue light applicable for fabrication of cool LEDs. LFPs visualized by staining optimized NPs following powder dusting technique exhibits well defined level 1-3 ridge characteristics. Hence, it evidences versatility of the development techniques and NPs for visualization of LFPs with excellent sensitivity, selectivity, and without background hindrance. The obtained results evidence that the optimized NPs can be explored as a novel labeling marker for probing visualization of LFPs and solid state lightning.

Keywords: Solvothermal, Photoluminescence, Latent fingerprint, Sweat pores.

1. Introduction

Now a day, fabrication and characterization of NPs creates numerous interests for scientific community owing to their excellent physical and chemical properties, which consequence of nano-regime [1-3]. Among the rare earth (RE) ions induced nano-sized inorganic phosphors exhibits exceptional thermal nature, chemical stability and excellent PL quantum efficiency.

White light-emitting diodes (WLEDs) have considered being next generation solid state lightning technology because of its highly luminous competence, long life time, less energy consumption, harmlessness, simple production, high stability and environmental safety [4-8].

Perovskite structured Barium titanates ($BaTiO_3$) have been extensively studied due to its outstanding dielectric and ferroelectric properties. Generally barium titanate was fabricated by solid-state reaction using barium carbonate and titanium dioxide as precursors at high temperature (1100 °C). The powders thus obtained were often low in purity and consist of large and non-uniform particles [9-11]. In order to overcome from these difficulties, a simple solvothermal method was adopted due to its major advantages namely energy saving, straight forwardness, superior nucleation control, elevated rate of reaction, better shape control, and etc. Further, several reasons for choosing this host includes, the production of fine particles with a narrow size distribution, the direct preparation of crystalline $BaTiO_3$ without high temperature calcination, the presence of powders not required to be milled before sintering, thus avoiding contamination, and the production of required morphology.

Fingerprints (FPs) were considered to be a vital source for identification of individuals in advanced forensic investigation. The ridge patterns on human fingers tips were unique and remain persists in whole lifespan. Majority of FPs commonly found during crime investigation was latent; hence efficient techniques were essential to visualize such LFPs [12-16]. Many efforts including both chemical as well as physical techniques have been followed to visualize LFPs. Nevertheless, many development methods have disadvantages including little sensitivity, elevated surroundings hindrance, complicated experimental procedure, and many hazardous. Due to these drawbacks the visualization ability was limited only level 1 - 2 ridge characteristics. In recent years the level 1 - 2 ridge characters were counterfeited by synthetic skin marks.

Therefore, visualization of level 3 (i.e., sweat pores) creates numerous interests for researchers [17]. Simple powder dusting method with efficient NPs having uniform particle size and morphology was considered to be an innovative advancement for visualization of LFPs with well defined superior quality ridge details was essential for personal identification during investigation [18-21]. Therefore, NPs which can reveal clear sweat pores have wide scope of applications in forensic analysis [22-24].

In the present study, $BaTiO_3:Nd^{3+}$ (1-11 mol %) broom-like hierarchical structures were fabricated via simple solvothermal method using CTAB as surfactant. Further, the morphological changes with various reaction parameters such as, synthesis temperature, surfactant concentration, time duration and pH of the precursor solution were systemically studied. The optimized NP was used to visualize LFPs on various porous and non-porous surfaces by following powder dusting technique.

2. Experimental

2.1 Materials used

The chemicals used in the present communication were AR grade Barium nitrate [$Ba(NO_3)_2$ (99.9 %)], Titanium (IV) isopropoxide [$Ti[OCH(CH_3)_2]_4$ (99.9 %)] [$Ti(C_4H_9O)_4$ (99.9 %)] and Neodymium nitrate [$Nd(NO_3)_3.5H_2O$ (99.9 %)] as oxidizers and Cetyl trimethylammonium bromide (CTAB) as surfactant.

2.2 Solvothermal synthesis of $BaTiO_3:Nd^{3+}$ (1-11 mol %) NPs

The $BaTiO_3:Nd^{3+}$ (1-11 mol %) NPs were fabricated by solvothermal route using *CTAB* as surfactant. Stoichiometric quantity of Barium nitrate, Titanium (IV) Isopropoxide and Neodymium nitrate were thoroughly dissolved in 20 ml ethanol using magnetic stirrer for ~ 10 min. Consequently, 5 ml of *CTAB* surfactant was mixed above precursor solution. The resultant

solution was transmitted to Teflon-lined autoclave (100 mL), sealed and maintained to ~ 180 °C for different reaction times (4 to 12 h) and cooled to room temperature. Similarly, experiment was repeated by varying experimental parameters, namely, concentration of CTAB, reaction temperature, and pH of the solution. Afterwards, samples were collected and cleaned by using double distilled water. The obtained samples were dried and calcined to ~ 800 °C. **Fig.1** shows the schematic representation of solvothermal synthesis of Nd^{3+} doped $BaTiO_3$ NPs.

2.3. Visualization of LFPs by staining $BaTiO_3$:Nd^{3+} (7 mol %) NPs.

All the LFPs were collected from single donor of age 26 year old male. The donor hands were thoroughly washed with soap water. Then, washed hands were dried in air, gently rubbed on forehead and deposited on various forensic related surfaces. The optimized $BaTiO_3$:Nd^{3+} (7 mol %) NP was carefully stained on LFPs and excess powder was removed by smooth brushing method. The LFPs were imaged by using 50 mm f/2.8G ED lens Nikon D3100/AF-S digital camera under UV 254 nm light.

2.3. Instruments used

Powder X-ray diffractometer (XRD, Shimadzu 7000) provided with Cu k_α (1.541 Å) radiation and nickel filter was used to study structural characterization of the prepared samples. Morphological features of the prepared products were studied using Hitachi table top (TM 3000) and Hitachi H-8100 equipped with EDS (Kevex sigma TM Quasar, USA). Perkin Elmer (35λ) spectrometer was used to record the diffuse reflectance spectroscopic data of the NPs. PL excitation and emission data was recorded using Jobin Yvon Spectroflourimeter Fluorolog-3 operational with 450W Xenon lamp as an excitation source.

3. Results and discussion

3.1 Structural analysis

The PXRD patterns of the synthesized $BaTiO_3:Nd^{3+}$ (1-11 mol %) NPs were depicts in Fig. 2 (a). The intense and narrow single diffraction peaks of PXRD patterns confirm single phase and were good agreement with standard JCPDS 74-1961 [25]. The acceptable percentage difference (D_r) between Ba^{2+} and Nd^{3+} can be calculated by formula

$$D_r = \frac{R_s - R_D}{R_s} \text{ ---------- (1)}$$

where R_s and R_D ; radius of host site and substitute ions respectively. The estimated value of D_r was found to be ~ 29 % and accordance with acceptable percentage difference (30 %). Thus, it evidently indicates that the effective substitution of dopant Nd^{3+} ions in Ba^{2+} site in host lattice. Therefore no obvious evidence of dopant and impurities were observed in a PXRD results. The obtained results reveals that the dopant (Nd^{3+}) ions were influenced the crystal structure arrangement but tailored the lattice parameters due to the ionic radius mismatch. Line broadening in prominent peaks was utilized to estimate average crystallite size (D) by following Scherrer's relation [26]:

$$D = \frac{0.9\lambda}{\beta \cos\theta} \text{ ---------- (2)}$$

where λ ; wavelength of X-rays, θ ; the Bragg's angle and β; full width half maxima (FWHM). The value of D was estimated and tabulated in Table.1. Broadening in the peaks was usually coupled with crystallite size (D) or strains within the sample or sometimes both. Therefore, the value of D and micro strain of the NPs were calculated using Williamsons Hall (W-H) equation as follows;

$$\frac{\beta \cos\theta}{\lambda} = \frac{1}{D} + \frac{\varepsilon \sin\theta}{\lambda} \text{ ---------- (3)}$$

where D ; crystallite size (nm), λ; the wavelength of used Cu kα radiation, β; FWHM of peak and θ; Bragg's diffraction angle. The value of D and strain were calculated and listed in Table 1. The W- H plots of the prepared samples as shown in Fig. 2(b).

3.2 Diffuse reflectance studies

Fig.3 depicts the diffuse reflectance spectra (DRS) of the pure and Nd^{3+} doped $BaTiO_3$ NPs at RT. It can be observed from the figure that, a weak absorption band at shorter wavelength was due to the meta-stable states formation between the valence band and conduction band by the dopant ions [27].

The spectra exhibit a broad peak at ~ 385 nm which may due to electron transitions from valence to conduction band. The other peaks at ~ 275, 360, 529, 586, 680,742 and 806 nm were due to $^4I_{9/2} \rightarrow {}^2F_{5/2}$, $^4D_{3/2}+{}^4D_{5/2}+{}^2I_{11/2}$, $^2K_{13/2}+{}^4G_{7/2}+{}^4G_{9/2}$, $^4G_{5/2}+{}^2G_{7/2}$, $^4F_{7/2}+{}^4S_{3/2}$, $^4F_{5/2}+{}^2H_{9/2}$ and $^4F_{3/2}$ transitions of Nd^{3+} ions respectively [28].

The energy band gap (E_g) of the prepared NPs can be estimated by applying the Kubelka–Munk (K-M) theory to DR spectra. The plots of $[F(R_\infty)h\nu]^{1/2}$ versus photon energy ($h\nu$) was shown in Fig 3. The Kubelka–Munk function F (R_∞) and photon energy ($h\nu$) was estimated by using the relations:

$$F(R_\infty) = \frac{(1-R_\infty)^2}{2R_\infty} \text{ ---------- (4)}$$

$$h\nu = \frac{1240}{\lambda} \text{ ---------- (5)}$$

where R_∞; reflection coefficient of the sample, λ; the absorption wavelength. The estimated band gap was found to be in range ~ 3.29-3.42 eV and given in Table. 1. The degree of structural order and disorder into the matrix was leads to changes in E_g and also which will change the distribution of energy levels within the band gap [14, 29].

3.3 Morphological studies

Effects of solvothermal temperature (100, 120, 150 and 180 ^oC) on the morphologies were systematically studied. When the solvothermal temperature maintained at 100 °C, uniform free-

standing needle type rods were obtained (Fig.4 (a)). Once the temperature was increased from 120 - 150 °C, free-standing needle shaped morphologies converted to broom-like bud microstructures were obtained (Fig.4 (b, c)). However, with increase of solvothermal temperature to 180 °C, all the microrods were overlapped with each other forming broom-like structures (Fig.4 (d)). Thus, it was clear that the solvothermal temperature can greatly affect the morphology of the product. Fig.4 (e-h) shows the influence of pH on the morphological features of $BaTiO_3$:Nd^{3+} (7 mol %) NPs. When pH was set to 3, free-standing uniform micro-rods were obtained (Fig.4 (e)). However, when pH was increased to 5 and 7, each rod having open end to form bullet shaped tips (Fig.4 (f, g)). When the pH was set to 9, bullet shaped tips were opened up and forms a flower-like morphology (Fig.4h).

Growth mechanism of broom-like and flower-like superstructures of $BaTiO_3$:Nd^{3+} (7 mol %) NP was shown in Fig.4. Usually, growth mechanism of superstructures involves two processes namely, nucleation and growth which main depends on concentration of precursors and reaction rate. Environmental conditions including acidic or basic nature of the precursors induces the formation of nuclei which further grow leads to microstructures. In the present work, at pH < 7 results rod shaped nuclei and it undergo orientated attachment leads to micro rod-like structures. Morphological evidence clearly demonstrates that acidic environment of the precursors favors the formation of superstructures, while basic nature (pH > 7) results the formation of irregular shaped micro particles.

The surfactant CTAB can play a vital role as template, driving the micro particles to aggregate or assemble in parallel or in a perpendicular arrangement. Thus, surfactant contributes to the formation of large-sized microrods by oriented assembly. The effect of CTAB concentration (5 - 20 ml) on the morphology was studied (Fig.4 (i-l)). When the CTAB

concentration was ~ 5 ml, non-uniform micro rods with different size were obtained (Fig.4 (i)). When the concentration of CTAB was increased to 10 ml, non-uniform with sharp tip microrods were oriented in uni-direction (Fig.4 (j)). When the CTAB concentration was further increased to 15 and 20 ml, an open and tapered tip micro rods were obtained (Fig.4 (k, l)). The effect of reaction time duration (12, 24, 36 and 48 h) on morphology was also studied (Fig.4 (m-p)). When the solvothermal reaction time was set to 12 h, uniform vertical microrods with broom-like morphology were obtained (Fig.4 (m)). When the reaction time was set to 24 h, microrods with sharp bullet-like tips were obtained (Fig.4 (n)). Further, increase in reaction time to 36 h; induces a broom-sticks which were tightly packed to each other (Fig.4 (o, p)). Fig.5 shows the tentative schemes to understand the formation of broom-like $BaTiO_3$:Nd^{3+} (7 mol %) NPs for various experimental conditions.

Growth mechanism

The surfactant CTAB concentration assisted growth mechanism of broom-like morphology was depicted in Fig.6. The hierarchical structures were mainly influenced by distance of separation between nucleation spots and driving force. At lower CTAB concentrations, concentric diffusion field induce around the crystal may due to rapid absorption by surface of crystals. However, at higher CTAB concentrations, But at higher concentrations of CTAB, the crystals tip project into diffusion layer and offers rapid growth than core regions of facets results the formation of elongated structures [30, 31]. Similarly cationic surfactant CTAB which form micelles with the preliminary formed $BaTiO_3$ NPs. In this study, the long aliphatic cetyl chain and polar trimethylammonium bromide become interior and exterior. The exterior polar trimethylammonium bromide attached to the polar $BaTiO_3$ to form hierarchical broom-like structures (Fig.6).

3.4 Photoluminescence studies

Fig.7 (a) depicts the excitation spectra of $BaTiO_3$: Nd^{3+} (7 mol %) NPs under 541 nm wavelength. The spectra exhibit broad peaks at ~ 395 and 470 nm. Among ~ 395 nm can be attributed to charge transfer (CT) from $O^{2-} \rightarrow Nd^{3+}$ peak. The position of CT peak was calculated by following Jørgensen equation [32].

$$E_{CT} = [\chi(L) - \chi(M)](3\times10^4) \text{---------- (7)}$$

where E_{CT} ; position of the CT band in cm^{-1}, $\chi(L)$ and $\chi(M)$; opto-electro negativities of the O^{2-} and Nd^{3+} cations respectively. The position of CT peak was calculated and found to be ~ 400 nm. The calculated value of position of CT peak (~ 400 nm) was good agreement with experimental value.

The PL emission spectra of $BaTiO_3$: Nd^{3+} (1-11 mol %) NPs excited at 395 nm were shown in Fig.7 (b). The spectra exhibits intense peaks at ~ 495, 542, and 613 nm attributed to $^2G_{9/2} \rightarrow {}^4I_{9/2}$, $^4G_{5/2}+{}^2G_{7/2} \rightarrow {}^4I_{9/2}$, and $^2H_{11/2} \rightarrow {}^4I_{9/2}$ transitions of Nd^{3+} ions, respectively [33]. Variation of PL intensity with concentration of Nd^{3+} ions was shown in Fig.7 (c). It evident that, the PL intensity increases upto 7 mol % of Nd^{3+} ions and afterwards diminishes due to phenomenon of concentration quenching. The electric multipolar interaction between Nd^{3+} ions was estimated by utilizing Van Uitert's relation [34];

$$\frac{I}{\chi} = K\left[1+\beta(\chi)^{\frac{Q}{3}}\right]^{-1} \text{---------- (8)}$$

where, χ ; dopant concentration (Nd^{3+}), Q ; a constant (Q= 3, 6, 8 and 10 specifies electric multipolar interactions namely, dipole – dipole (d - d), dipole – quadrupole (d - q) and quadrupole – quadrupole (q - q) interactions and K & β ; constants. Fig.7 (d) shows log (x) v/s log (I/x) plot of $BaTiO_3$:Nd^{3+} (1-11 mol %) NPs. The obtained value of Q was found to be ~

7.18, which was good agreement with theoretical value (i.e., Q = 8). This specifies that q-q interaction mechanism which leads to concentration quenching in $BaTiO_3:Nd^{3+}$ (1-11 mol %) NPs.

The J–O theory was necessary tool for studying the PL properties of RE ions doped NPs [35] using experimental PL emission results. The J-O optical transition parameters (Ω_2 and Ω_4) were estimated by least-squares fitting approach between measured and calculated line strengths (S_{meas} and S_{cal}).

$$A_T = \frac{64\Pi^4 \nu^3 e^2}{3hc^3} \frac{1}{4\Pi\varepsilon_0} \chi \sum_{J=4,6} \Omega_J \left\langle {}^1D_0 \left| U^{(J)} \right| {}^3F_4 \right\rangle^2 \quad \text{---------- (9)}$$

where ν ; average transition energy (cm^{-1}), h ; Planck's constant (6.63×10^{-27} erg s), J ; angular momentum of initial level in the transition, $\chi = n(n^2 + 2)^2 /9$; local field correction factor, *e;* elementary charge and $\left\langle {}^1D_0 \left| U^{(J)} \right| {}^3F_4 \right\rangle$; doubly reduced matrix elements of the tensor operator U^J. The J–O parameters (Ω_2 and Ω_4) of BaTiO3:Nd^{3+} (1-11 mol %) NPs were estimated and tabulated in Table 2. The variation in the value of Ω_2 shows highly sensitive with ligand environment, while Ω_4 was related to long-range effect.

The other radiative properties namely transition probabilities (A_T), radiative lifetime (τ_R) and branching ratios (β_R) of the excited states of Nd^{3+} were calculated by using J–O parameters. The A_T for a transition $J \to J'$ was calculated from by an equation [36].

$$A_T(J \to J') = \frac{64\pi^4 \upsilon^3 e^2}{3h(2J+1)} \left[\frac{n(n^2+2)^2}{9} S_{ed} + n^3 S_{md} \right] \text{---------- (10)}$$

The radiative lifetime (τ_R) and branching ratios was given by

$$\tau_R(J) = \frac{1}{\sum_{\psi J'} A_T(J \to J')} \text{ ---------- (11)}$$

$$\beta_R(J, J') = \frac{A_T(J \to J')}{\sum_{J'} A_T(J \to J')} \text{ ---------- (12)}$$

The radiative properties of Nd^{3+} doped $BaTiO_3$ NPs were estimated and given in Table 2.

The CIE chromaticity and correlated color temperature (CCT) diagram of $BaTiO_3$:Nd^{3+} was shown in Fig. 7 (e & f). The calculated values of CIE co ordinates of the $BaTiO_3$:Nd^{3+} (1-11 mol %) NPs were tabulated in Table 3. The CIE diagram clearly evidences that, the estimated co ordinates were located in blue and tuned towards pure blue region. The CCT values were estimated by transforming CIE co-ordinates to (U', V'), as follows [37];

$$U' = \frac{4x}{-2x + 12y + 3} \text{ ---------- (9)}$$

$$V' = \frac{9y}{-2x + 12y + 3} \text{ ---------- (10)}$$

The calculated values of CCT were in the range of ~ 10000-11000 K and values were listed in Table 3. Therefore, the present NPs were highly useful for the production of cool blue light in WLEDs and solid state display applications.

3.5 Visualization of LFPs

Fig.8 shows the visualize LFPs on non-porous surfaces such as highlighter, marker, spatula, CD, glass slide, TV remote, battery charger and spray bottle by staining optimized $BaTiO_3$:Nd^{3+} (7 mol %) NPs under 254 nm UV light. The results clearly evident that, well defined ridge details including all three levels were clearly visualized due to its nano regime and better adhesion nature.

Understanding of surface porosity was very important aspect for choice of visualization technique because it can strongly determine constituents of the FPs which were available during impression. Usually, FP residue was a constituent of water and lipid soluble emulsion, which varies based on the type of the substrate [38]. For visualization of LFPs, surfaces were commonly cited in one of three groups namely porous, non-porous and semi-porous. Porous surfaces, namely as paper, cardboard and wood, were rapid absorptive of FPs residues after deposition. Water-soluble chemical constituents of FPs such as amino acids, urea and chlorides were absorbed within few seconds and as water evaporates constituents were left on the surface. These constituents can stay longer period on the surface as they were confined from mechanical stress, and visualization techniques. The penetration depth was mainly depends on the porosity level of the surface and size of each chemical constituent. In addition, surrounding environmental conditions namely temperature and humidity will also contribute to initial penetration.

However, non-porous surfaces such as plastics, glass and marbles do not absorb any chemical constituent of FP. Because both water- and lipid-soluble constituents can be accessible indefinitely until they evaporate or degrade. These constituents will readily undergo degradation in the form mechanical stress and environmental weathering. Further, the semi-porous surface lies in between porous and non-porous surfaces. For example currencies and magazine covers were major examples of semi-porous surfaces, which absorb constituents at a slower rate than porous surfaces. In the present work, we work out visualization of LFPs on various porous, semi-porous and non-porous surfaces using optimized $BaTiO_3:Nd^{3+}$ (7 mol %) NP.

To determine background hindrance of optimized $BaTiO_3:Nd^{3+}$ (7 mol %) NPs based LFPs visualization, a sequence of complex porous surfaces including playing cards, magazine,

spray bottle surfaces were chosen and where impressions were printed, stained by the optimized NP and then visualized under 254 nm UV light as shown in Fig.9. LFPs were clealry visible without any background inteference after UV light irradiation, ensuing in exceptional contrast for enhanced LFP visualization. Fig.10 shows the fingerprint ridge characteristics developed on the glass surface under 254 nm UV light. As it can be observed from the figure that, all the three levels (whorl, ridge end, bi-furcation, cross-over, eye, island and sweat pores) of ridge details were clearly visualized.

Due to surface reactions, diverse decomposition, and oxidative mechanisms, the chemical constituent of LFPs was significantly inconsistent. Generally, compositions of LFPs can be classified into two types: (i) the initial composition, at deposition chemical constituents present in fingertip was transferred to the surface and (ii) the aged composition, containing the existing initial constituents and degradation products. A little research has been required to identify the changes between the initial and aged compositions and the rate of change with time (Fig.11a). Therefore, in the present work, we conducted series of experiments with different LFP aging to demonstrate the practicability of the optimized $BaTiO_3:Nd^{3+}$ (7 mol %) NP on aluminum foil surface under UV 254 nm light. The detection sensitivity gradually decreased with increasing aging of the LFPs, due to the gradual evaporation of the LFP constituents was observed [39].

However, to determine the efficiency of optimized NPs, the LFPs on aluminum foil were maintained at various temperatures (30 to 45 ^{o}C) for ~ 1 h (Fig.11b). From the figure it was observed that visualized LFP maintained at ~ 30 ^{o}C exhibits sharp well defined ridge patterns and reveals level 1 and level 2 details. However, faint FP patterns were observed, when temperature was increases to 40 ^{o}C. Further, when the temperature was increased to 45 ^{o}C the ridge patterns were completely disappeared due to evaporation of biogenic constituents of LFPs.

To evaluate the sensitivity and selectivity of LFPs were visualized using optimized NPs on various fruits and vegetables namely green apple, capsicum and cucumber under 254 nm light (Fig.12). These fruits and vegetables subjected to deterioration depends on environmental and storage conditions (e.g., temperature and humidity). The obtained results evident that the apple and capsicum exhibits defined ridges due to its smooth and longer shelf life. However, the surface of cucumber has also soft and moisture containing surface hence partial prints was visualized. Similarly, glassy and smooth surfaced tomato shows less clarity FPs due its color interference. On the other hand, visualization of LFPs on the onion and potato surfaces was achieved using optimized NPs, but only level 1 detail can be enhanced due their contrast colors [40].

Further, series of physical abrasions test was performed on various surfaces including highlighter pen and compact disc before and after abrasion under 254 nm light to investigate external abrasions can destroy FPs visualization (Fig.13). The obtained results indicate that the visualized LFPs using prepared sample exhibits clear ridge details even after II scratch [41].

Aforementioned results evidence that the successfully tailored blue light emitting NPs to visualize LFPs using novel powder dusting technique on most neglected various porous, semi-porous and non – porous surfaces under UV 254 nm light. Visualized LFPs exhibits high efficiency (since visualization procedure was rapid and it requires ~ 2 min for trained professionals) and high sensitivity (due to lower background hindrance).

4. Conclusions

Blue light emitting $BaTiO_3:Nd^{3+}$ NPs were successfully prepared by CTAB surfactant assisted solvothermal route. The morphology of the product was highly dependent on various solvothermal reactions such as, temperature, concentration of CTAB, pH and reaction time duration. The PL emission spectra exhibits emission peaks at 495, 542, and 613 nm attributed to to $^2G_{9/2} \rightarrow {}^4I_{9/2}$, $^4G_{5/2}+{}^2G_{7/2} \rightarrow {}^4I_{9/2}$, $^2H_{11/2} \rightarrow {}^4I_{9/2}$ and $^4H_{9/2} \rightarrow {}^4I_{9/2}$ transitions of Nd^{3+} ions, respectively. The CIE and CCT results indicate that the phosphor exhibit intense blue light applicable for fabrication of cool LEDs. The optimized product was successfully explored as efficient labeling agent for visualizing LFPs on various porous and non-porous surfaces. Owing to nano regime and good adherence efficiency, LFPs were visualized with high sensitivity, low background hindrance, high efficiency, and low toxicity. Therefore, the obtained NPs could be a definitive choice as advanced luminescent marker for multifunctional applications.

Acknowledgment

Dr.S.C. Sharma wish to thank DST-FIST NO.SR/FST/ETT-378/2014 for sanctioning of the project.

References

1. S. Verma, K. Verma, D. Kumar, B. Chaudhary, S. Som, V. Sharma, V. Kumar, H. C. Swart, Recent advances in rare earth doped alkali-alkaline earth borates for solid state lighting applications, Physica B, https://doi.org/10.1016/j.physb.2017.06.073.
2. M. Venkataravanappa, H. Nagabhushana, G.P. Darshan, S.C. Sharma, K.V. Archana, R.B. Basavaraj, B. Daruka Prasad, Facile ultrasound route for the fabrication of green emitting $Ba_2SiO_4:Eu^{2+}$ nanophosphors for display and dosimetric applications, Mater. Res. Bull. 97 (2018) 281-292.
3. M. Dhanalakshmi, H. Nagabhushana, G.P. Darshan, B. Daruka Prasad, Ultrasound assisted sonochemically engineered effective red luminescent labeling agent for high resolution visualization of latent fingerprints, Mater. Res. Bull. 98 (2018) 250-264.
4. C. Tong, Y. Zhu, C. Xu, L. Yang, Y. Lia, Luminescence properties and color identification of Eu doped $Ca_3(PO_4)_2$ phosphors calcined in air, Physica B. 521 (2017) 153-157.
5. Irish Valerie B. Maggay, Kai-Yuan Yeh, Bingfu Lei, Mikhail G. Brik, Michal Piasecki, Wei-Ren Liu, Luminescence properties of Eu^{2+}-activated $NaCaBeSi_2O_6F$ for white light-emitting diode applications, Mater. Res. Bull. 100 (2018) 26-31.
6. Dorim Kim, Sungwook Park, Byung Chun Choi, Sung Heum Park, Jung Hyun Jeong, Jung Hwan Kim, The tetravalent manganese activated $SrLaMgTaO_6$ phosphor for w-LED applications, Mater. Res. Bull. 97 (2018) 115-120.
7. Nisha Deopa, A.S. Rao, Ankur Choudhary, Shubham Saini, Abhishek Navhal, M. Jayasimhadri, D. Haranath, G. Vijaya Prakash, Photoluminescence investigations on Sm^{3+} ions doped borate glasses for tricolor w-LEDs and lasers, Mater. Res. Bull. 100 (2018) 206-212.
8. Qiang Ren, Fei Lin, Xiulan Wu, Ou Hai, Tengyue Wei, Yehui Jiao, Huanhuan Li, Synthesis and luminescent properties of $KGd(MoO_4)_2:Sm^{3+}$ red phosphor for white light emitting diodes, Mater. Res. Bull. 90 (2017) 66-72.
9. M. Laguna, A. Escudero, N.O. Nunez, A.I. Becerro, M. Ocana, Europium-doped $NaGd(WO_4)_2$ nanophosphors: synthesis, luminescence and their coating with fluorescein for pH sensing, Dalton Trans. 46 (2017) 11575-11583.
10. H. Li, G. Liu, J. Wang, X. Dong, W. Yu, Eu^{3+}/Tb^{3+} doped cubic BaGdF5 multifunctional nanophosphors: Multicolor tunable luminescence, energy transfer and magnetic properties, J. Lumin., 186 (2017) 6-15.
11. X. Huang, B. Li, H. Guo, D. Chen, Molybdenum-doping-induced photoluminescence enhancement in Eu^{3+}-activated $CaWO_4$ red-emitting phosphors for white light-emitting diodes, Dyes Pigm. 143 (2017) 86-94.
12. G.P. Darshan, H.B. Premkumar, H. Nagabhushana, S.C. Sharma, B. Daruka Prasad, S.C. Prashantha, R.B. Basavaraj, Superstructures of doped yttrium aluminates for luminescent and advanced forensic investigations, J Alloys Compd. 686 (2016) 577 – 587.
13. R.B. Basavaraj, H. Nagabhushana, G.P. Darshan, B. Daruka Prasad, S.C. Sharma, K.N. Venkatachalaiah, Ultrasound assisted rare earth doped Wollastonite nanopowders: Labeling agent for imaging eccrine latent fingerprints and cheiloscopy applications, J. Ind. Eng. Chem. 51 (2017) 90-105.
14. R.B. Basavaraj, H. Nagabhushana, G.P. Darshan, B. Daruka Prasad, M. Rahul, S.C. Sharma, R. Sudaramani, K.V. Archana, Red and green emitting CTAB assisted $CdSiO_3:Tb^{3+}/Eu^{3+}$

nanopowders as fluorescent labeling agents used in forensic and display applications, Dyes Pigm. 147 (2017) 364-377.

15. K.N. Venkatachalaiah, H. Nagabhushana, G.P. Darshan, R.B. Basavaraj, B. Daruka Prasad, Novel and highly efficient red luminescent sensor based $SiO_2@Y_2O_3:Eu^{3+}$, M^+ (M^+ = Li, Na, K) composite core–shell fluorescent markers for latent fingerprint recognition, security ink and solid state lightning applications, Sens. Actuators, B. 251 (2017) 310-325.
16. V. Sharma, A. Das, V. Kumar, O.M. Ntwaeaborwa, H.C. Swart, Potential of $Sr_4Al_{14}O_{25}$: Eu^{2+}, Dy^{3+} inorganic oxide-based nanophosphor in Latent fingermark detection, J Mater Sci. 49 (2014) 2225–2234.
17. D. Park, B.J. Park, J. Kim, Hydrochromic Approaches to Mapping Human Sweat Pores, Acc. Chem. Res. 49 (2016), 1211−1222.
18. J.Y. Park, H.K. Yang, Novel red-emitting $Y_4Zr_3O_{12}:Eu^{3+}$ nanophosphor for latent fingerprinting technology, Dyes Pigm. 10.1016/j.dyepig.2017.02.036.
19. J. Graham, R.J. McNicol, K. Greig, W.T. G. Van De Ven, Identification of red raspberry cultivars and an assessment of their relatedness using fingerprints produced by random primers, J. Hortic. Sci. 69 (1994) 123-130.
20. P. Theys, Y.Turgis, A. Lepareux, G. Chevet, F. Ceccealdi, New Technique for Bringing Out Latent Fingerprints on Paper: Vacuum Metallization. Int. Crim. Pol. Review. 217 (1968) 106-108.
21. G.S. Sodhi, J. Kaur, Powder method for detecting LFPs: A review, Forensic Sci. Int. 120 (2001) 172 – 176.
22. M. Trapecar, M.K. Vinkovic, Techniques for fingerprint recovery on vegetable and fruit surfaces used in Slovenia - A preliminary study, Sci. Justice. 48 (2008) 192-195.
23. M. Wang, M. Li, M. Yang, X. Zhang, A. Yu, Y. Zhu, P. Qiu, C. Mao, NIR-induced highly sensitive detection of latent fingermarks by $NaYF_4$: Yb, Er upconversion nanoparticles in a dry powder state, Nano Res. 8 (2015) 1800–1810.
24. A. Sandhyarani, M.K. Kokila, G.P. Darshan, R.B. Basavaraj, B. Daruka Prasad, S.C. Sharma, T.K.S. Lakshmi, H. Nagabhushana, Versatile core-shell $SiO_2@SrTiO_3:Eu^{3+}$, Li^+ nanopowders as fluorescent label for the visualization of latent fingerprints and anti-counterfeiting applications, Chem. Eng. J. 327 (2017) 1135-1150.
25. D.K. Singh, K. M., J. Manam, Improved photoluminescence, thermal stability and temperature sensing performances of K^+ incorporated perovskite $BaTiO_3$: Eu^{3+} red emitting phosphors, Ceram. Intern. 43 (2017) 13602-13611.
26. R.B. Basavaraj, H. Nagabhushana, B. Daruka Prasad, S.C. Sharma, K.N. Venkatachalaiah, Mimosa pudica mediated praseodymium substituted calcium silicate nanostructures for white LED application, J. Alloys Compd. 690 (2017) 730-740.
27. G.P. Darshan, H.B. Premkumar, H. Nagabhushana, S.C. Sharma, B. Daruka Prasad, S.C. Prashantha, Neodymium doped yttrium aluminate synthesis and optical properties – A blue light emitting nanophosphor and its use in advanced forensic analysis, Dyes Pigm. 134 (2016) 227-233.
28. R.B. Basavaraj, H. Nagabhushana, B. Daruka Prasad, G.R. Vijayakumar, Zinc silicates with tunable morphology by surfactant assisted sonochemical route suitable for NUV excitable white light emitting diodes, Ultrason. Sonochem. 34 (2017) 700-712.
29. K. Kombaiah, J. Judith Vijaya, L. John Kennedy , M. Bououdina, Hamad A. Al-Lohedan, R. Jothi Ramalingam, Studies on Opuntia dilenii haw mediated multifunctional $ZnFe_2O_4$

nanoparticles: Optical, magnetic and catalytic applications, Mater. Chem. Phys. 194 (2017) 153-164.
30. S. Bari, A. Chatterjee, S. Mishra, Ultrasonication assisted and surfactant mediated synergistic approach for synthesis of calcium sulfate nano-dendrites, Ultrason. Sonochem. 31 (2016) 39-50.
31. H. Nagabhushana, R.B. Basavaraj, B. Daruka Prasad, S.C. Sharma, H.B. Premkumar, Udayabhanu, G.R. Vijayakumar, Facile EGCG assisted green synthesis of raspberry shaped CdO nanoparticles, J. Alloys Compd. 669 (2016) 232-239.
32. C. K. Jorgensen, "Electron Transfer Spectra", John Wiley & Sons, Inc., 1970.
33. M. Sahu, S.K. Gupta, R.M. Kadam, M.K. Saxena, Dopant Concentration induced optical changes in $Ba_{1-x}Eu_xMoO_4$: A green and facile approach towards tunable photoluminescent material, J. Lumin. 188 (2017) 67-74.
34. V. Venkataramu, P. Babu, C. K. Jayasankar, Th.Tröster, W. Sievers, G. Wortmann, Opt. Mater. 29 (2007) 1429-1439.
35. B. Judd, Estimation of chromaticity differences and nearest color temperature on the standard 1931 ICI colorimetric coordinate system, J. Deane, Opt. Soc. Am. 26 (1936) 421-426.
36. Kanchan Mondal, Puja Kumari, J. Manam, Influence of doping and annealing temperature on the structural and optical properties of $Mg_2SiO_4:Eu^{3+}$ synthesized by combustion method, Curr. Appl Phys. 16 (2016) 707-719.
37. K.N. Venkatachalaiah, H. Nagabhushana, G.P. Darshan, R.B. Basavaraj, B. Daruka Prasad, S.C. Sharma, Structural, morphological and photometric properties of sonochemically synthesized Eu^{3+} doped Y_2O_3 nanophosphor for optoelectronic devices, Mater. Res. Bull. 94 (2017) 442-455.
38. S. Cadd, M. Islam, P. Manson, S. Bleay, Fingerprint composition and aging: A literature review, Sci. Just. 55 (2015) 219-238.
39. R.S. Croxton, M.G. Baron, D. Butler, T. Kent, V.G. Sears, Variation in amino acid and lipid composition of latent fingerprints, Forensic Sci. Int. 199 (2010) 93-102.
40. L. Rae, D. Gentles, K.J. Farrugi, An investigation into the enhancement of fingermarks in blood on fruit and vegetables, Sci. Just. 53 (2013) 321–327.
41. S. Madkour, A. sheta, F. Badr El Dine, Y. Elwakeel, N. AbdAllah, Development of latent fingerprints on non-porous surfaces recovered from fresh and sea water, Egypt. J. Forensic Sci. (2017) 7:3.

Figure captions:

Fig.1. Schematic illustration for the solvothermal synthesis of $BaTiO_3:Nd^{3+}$ broom-like structures.

Fig.2. (a) PXRD patterns and **(b)** Williamson-Hall plots of $BaTiO_3:Nd^{3+}$ (1-11 mol %) NPs.

Fig.3. Band gap plots and diffuse reflectance spectra (Inset) of $BaTiO_3:Nd^{3+}$ (1-11 mol %) NPs.

Fig.4. SEM micrographs of $BaTiO_3:Nd^{3+}$ (7 mol %) NSs prepared under various reaction conditions. (a-d) temperature, (e, f) pH 3, 5, 7 and 11 (g-j) CTAB concentration and (m-p) time durations.

Fig.5. Tentative schemes to understand the formation of broom-like $BaTiO_3:Nd^{3+}$ (7 mol %) NSs under various reaction conditions.

Fig.6. Schematic representation of $BaTiO_3:Nd^{3+}$ (7 mol %) broom-like structures in the presence of CTAB surfactant.

Fig.7. (a) Excitation spectrum, **(b)** emission spectra, **(c)** PL intensity vs Nd^{3+} concentration plot, (d) log x vs log (I/x), **(e)** CIE and **(f)** CCT diagrams of $BaTiO_3:Nd^{3+}$ (1-11 mol %) NPs.

Fig.8. LFPs developed on the various non-porous surfaces using $BaTiO_3:Nd^{3+}$ (7 mol %) NSs under 254 nm UV light.

Fig.9. LFPs developed on the porous surfaces using $BaTiO_3:Nd^{3+}$ (7 mol %) NPs under 254 nm UV light.

Fig.10. Fingerprint ridge characteristics of $BaTiO_3:Nd^{3+}$ (7 mol %) NPs on the glass surface under 254 nm UV light.

Fig.11. LFPs developed on the surface of green apple, capsicum and cucumber using $BaTiO_3:Nd^{3+}$ (7 mol %) NPs under 254 nm UV light.

Fig.12 (a) aging of FPs on aluminum foil surface for different durations and (b) FPs stored at different temperatures

Fig.13 FPs abrasion test on various surfaces.

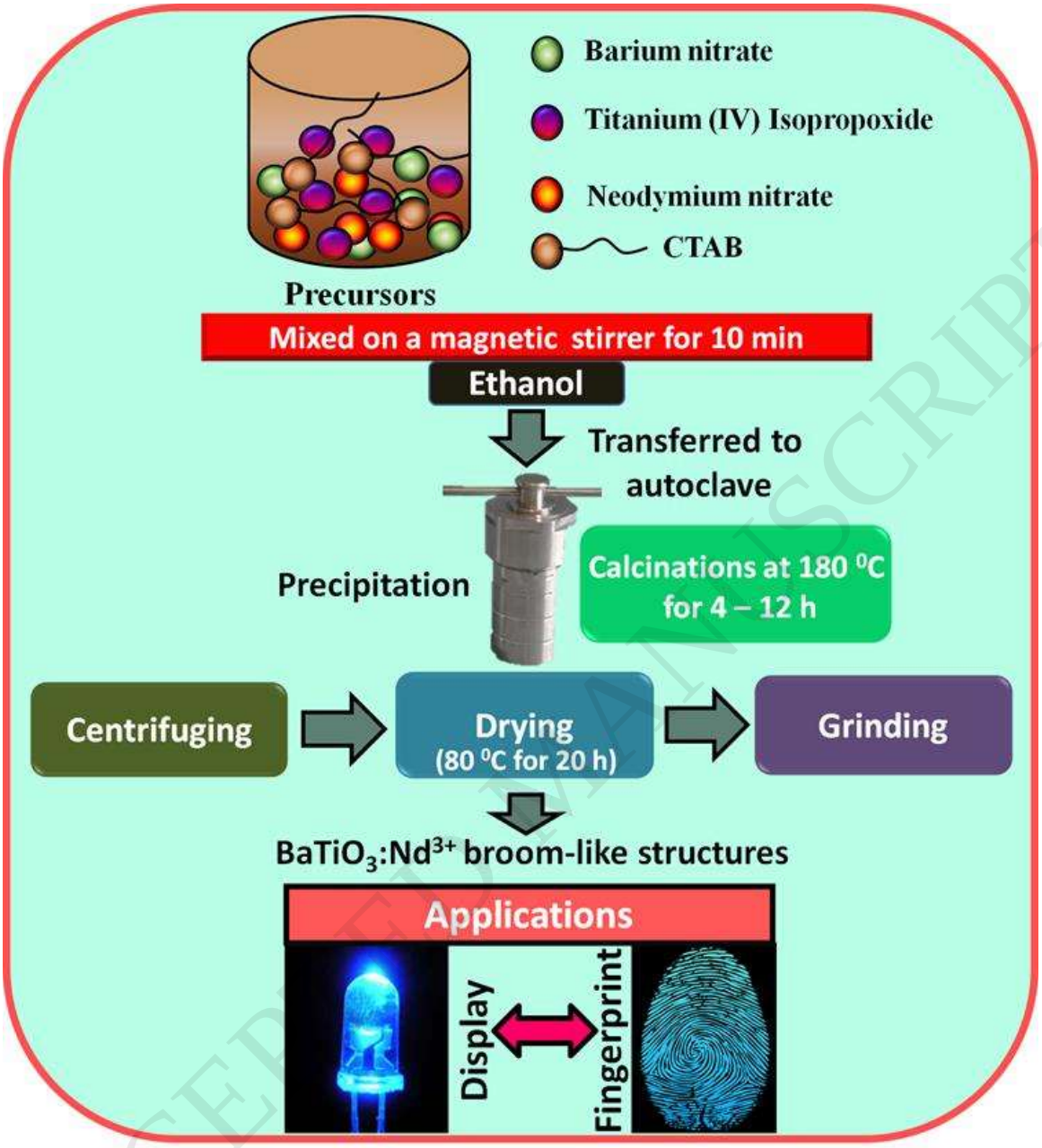

Fig.1. Schematic illustration for the solvothermal synthesis of $BaTiO_3:Nd^{3+}$ broom-like structures.

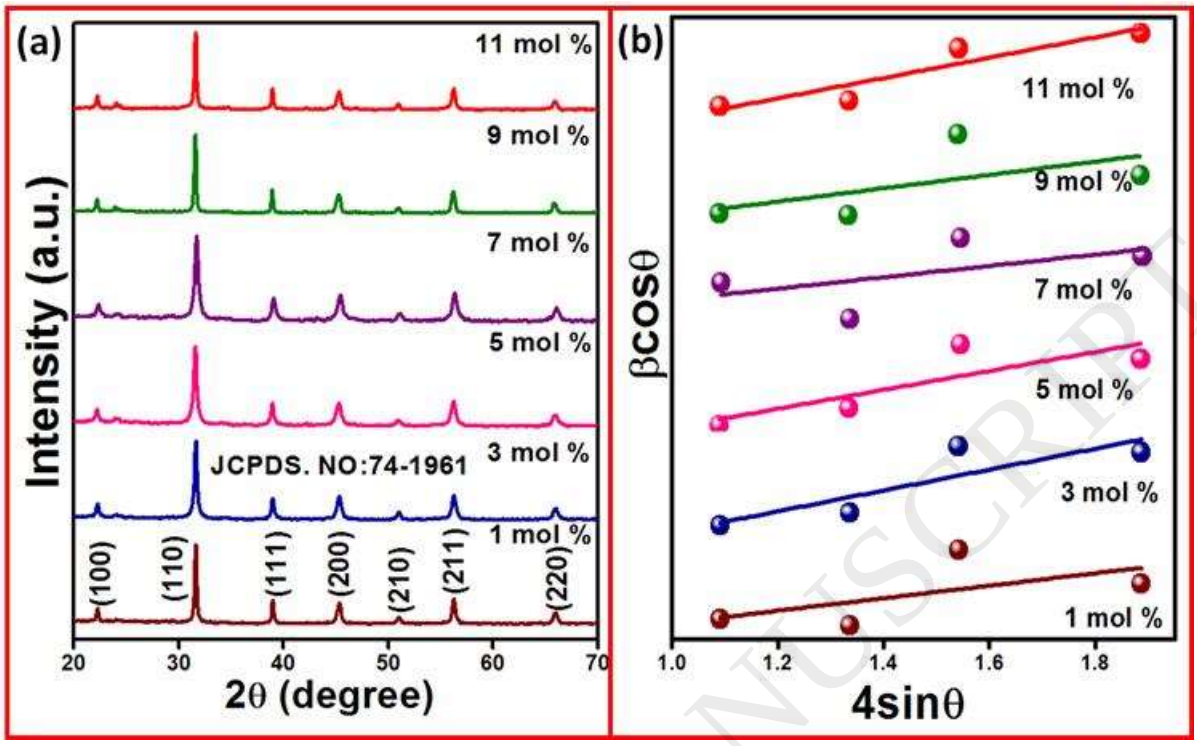

Fig.2. (a) PXRD patterns and **(b)** Williamson-Hall plots of $BaTiO_3:Nd^{3+}$ (1-11 mol %) NPs.

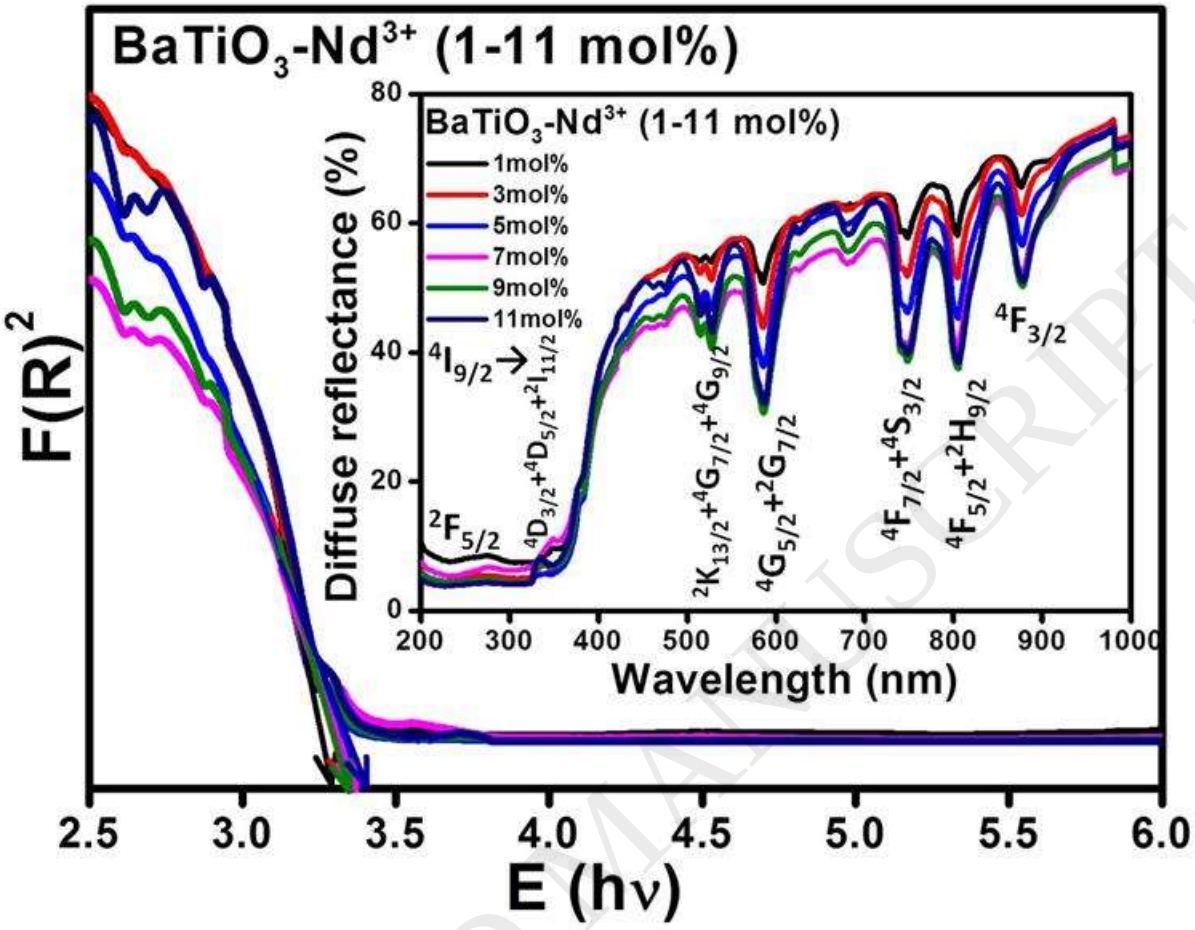

Fig.3. Band gap plots and diffuse reflectance spectra (Inset) of $BaTiO_3:Nd^{3+}$ (1-11 mol %) NPs.

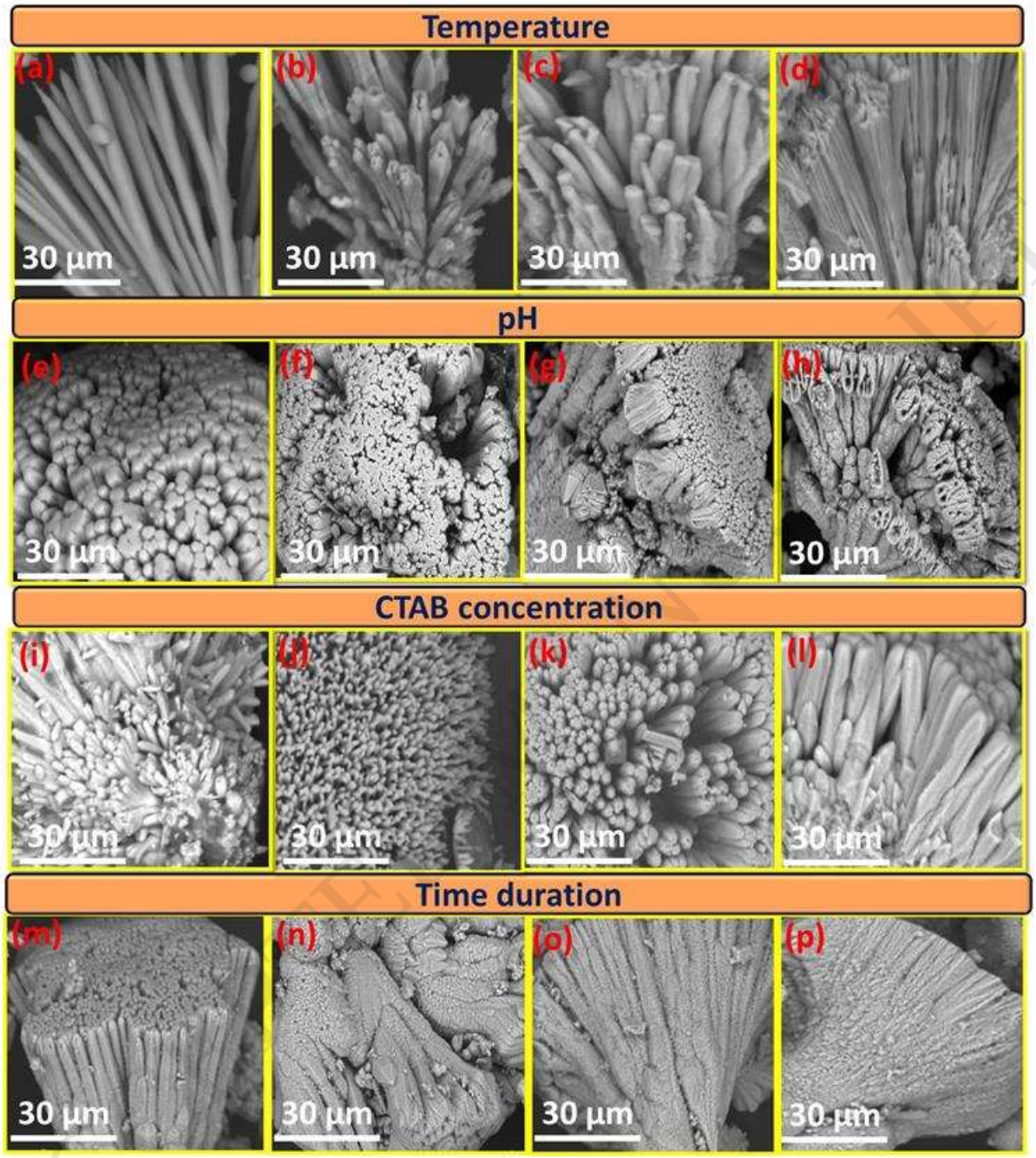

Fig.4. SEM micrographs of $BaTiO_3:Nd^{3+}$ (7 mol %) NSs prepared under various reaction conditions. (a-d) temperature, (e, f) pH 3, 5, 7 and 11 (g-j) CTAB concentration and (m-p) time durations.

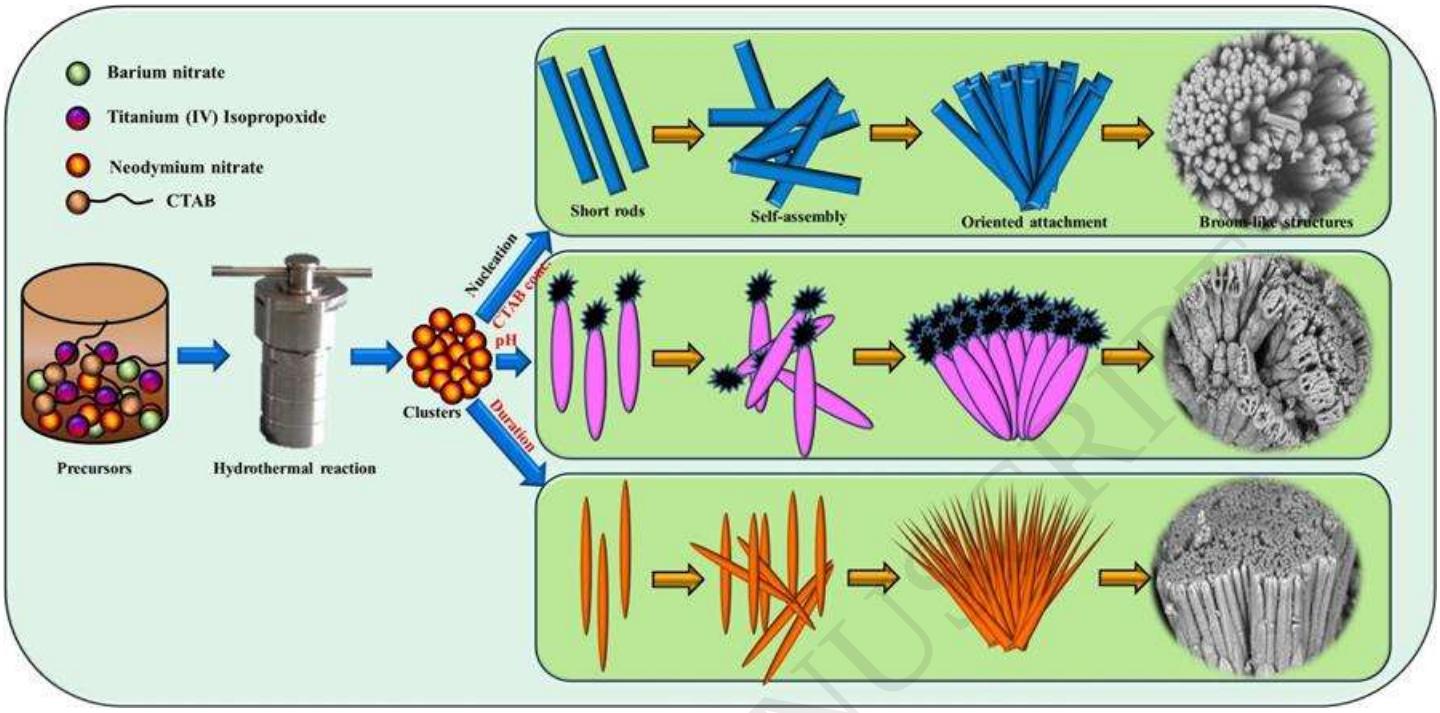

Fig.5. Tentative schemes to understand the formation of broom-like $BaTiO_3$:Nd^{3+} (7 mol %) NPs under various reaction conditions.

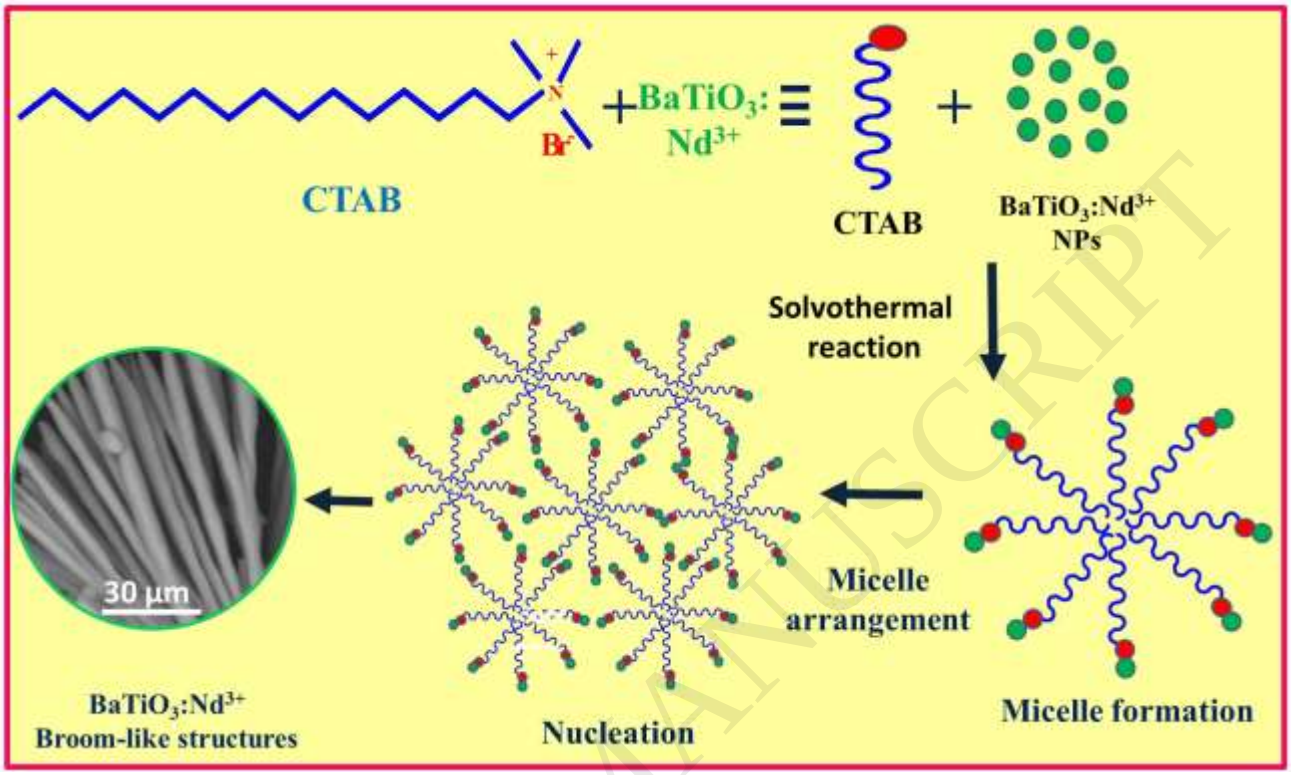

Fig.6. Schematic representation of $BaTiO_3:Nd^{3+}$ (7 mol %) broom-like structures in the presence of CTAB surfactant.

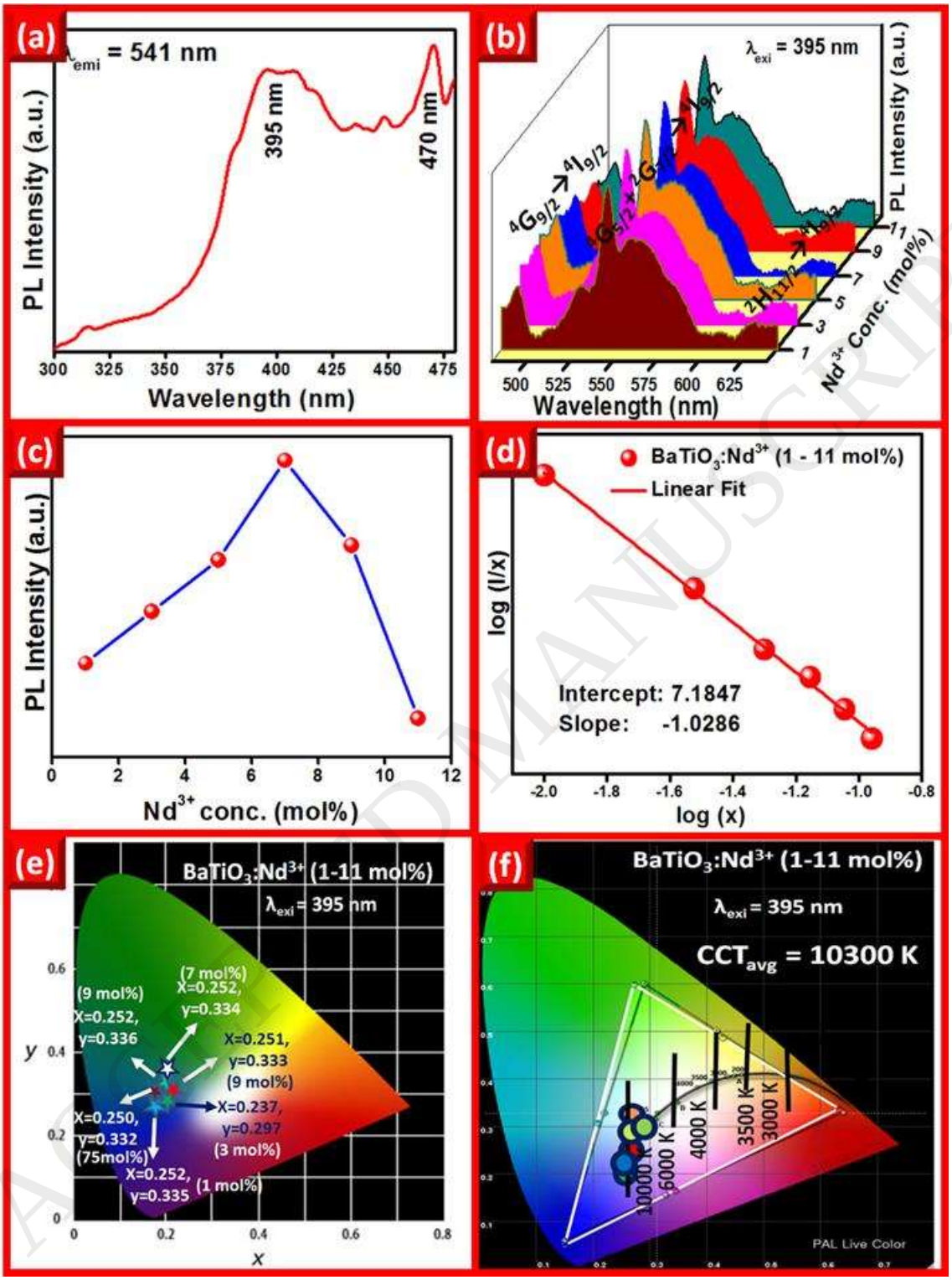

Fig.7. (a) Excitation spectrum, **(b)** emission spectra, **(c)** PL intensity vs Nd^{3+} concentration plot, (d) log x vs log (I/x), **(e)** CIE and **(f)** CCT diagrams of $BaTiO_3$:Nd^{3+} (1-11 mol %) NPs.

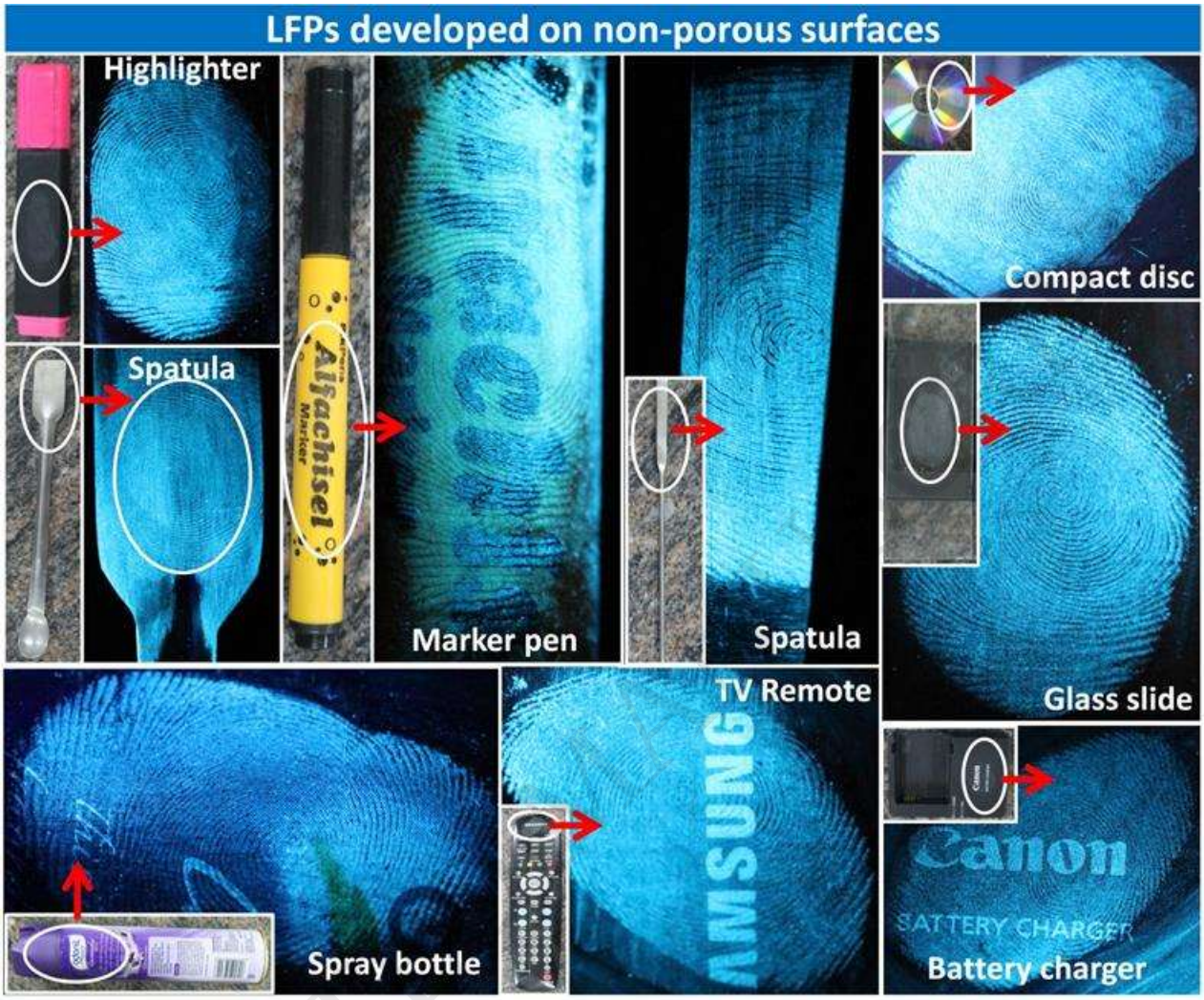

Fig.8. LFPs developed on the various non-porous surfaces using $BaTiO_3:Nd^{3+}$ (7 mol %) NSs under 254 nm UV light.

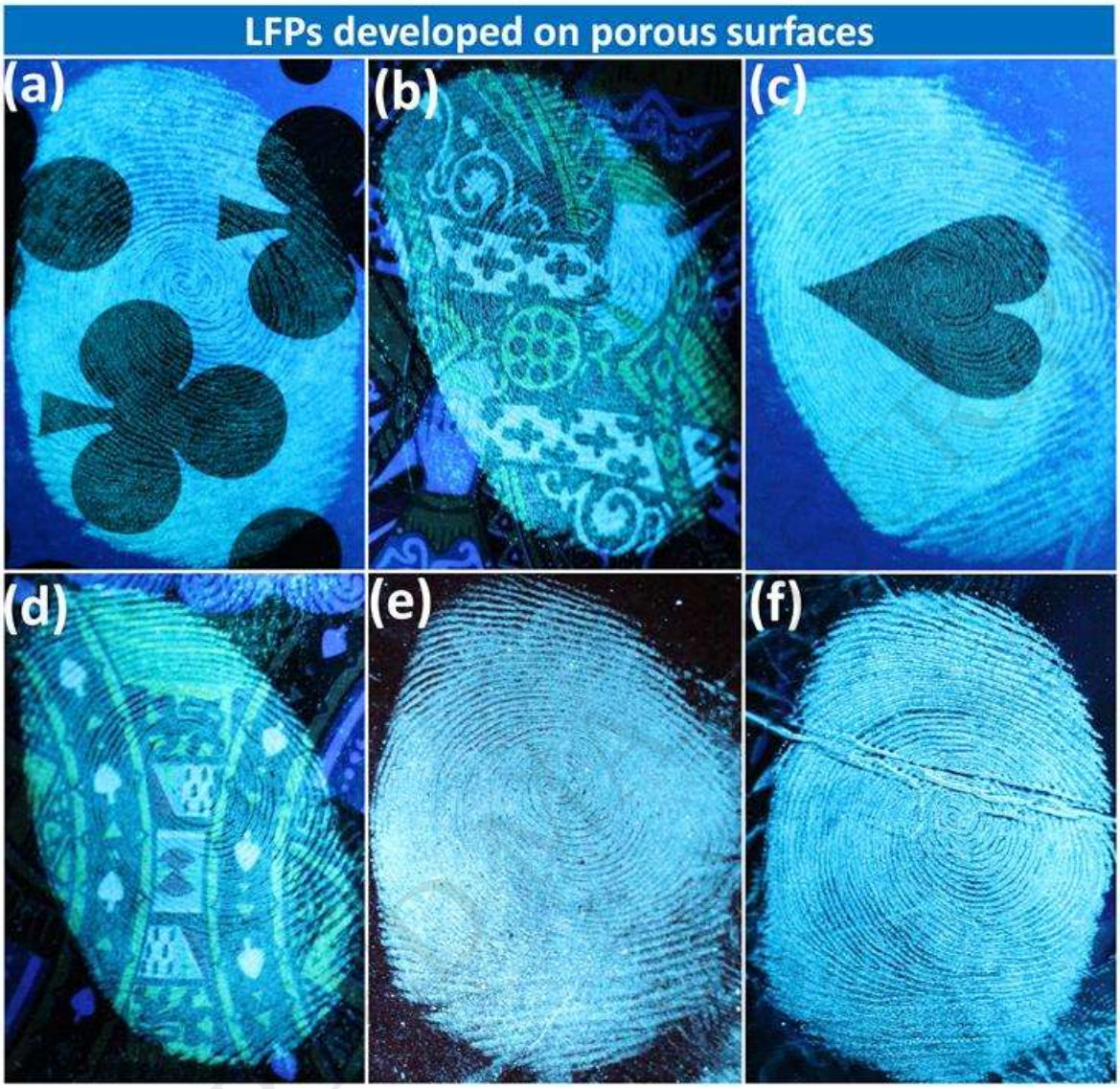

Fig.9. LFPs developed on the porous surfaces using $BaTiO_3:Nd^{3+}$ (7 mol %) NPs under 254 nm UV light.

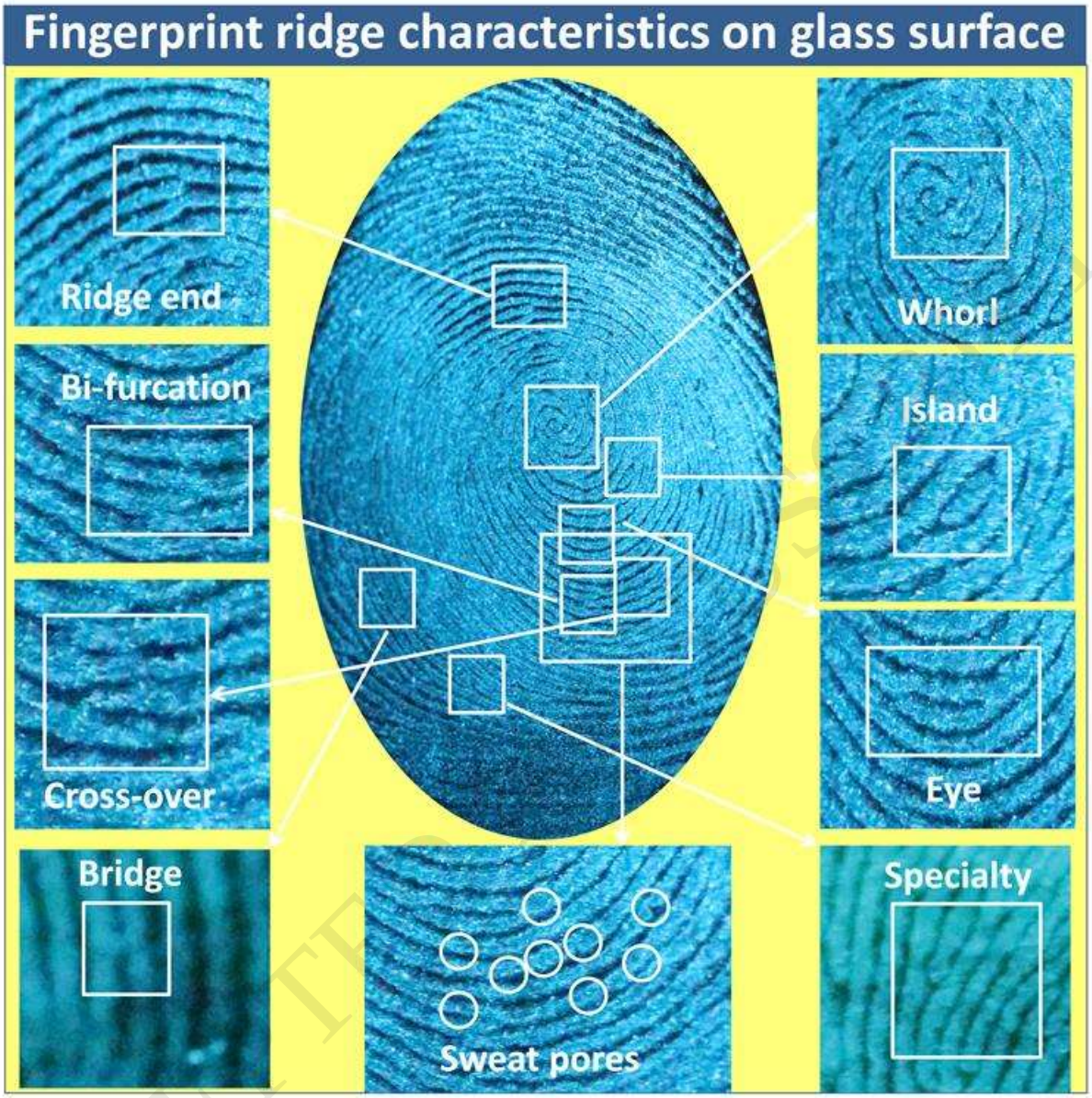

Fig.10. Fingerprint ridge characteristics of $BaTiO_3:Nd^{3+}$ (7 mol %) NPs on the glass surface under 254 nm UV light.

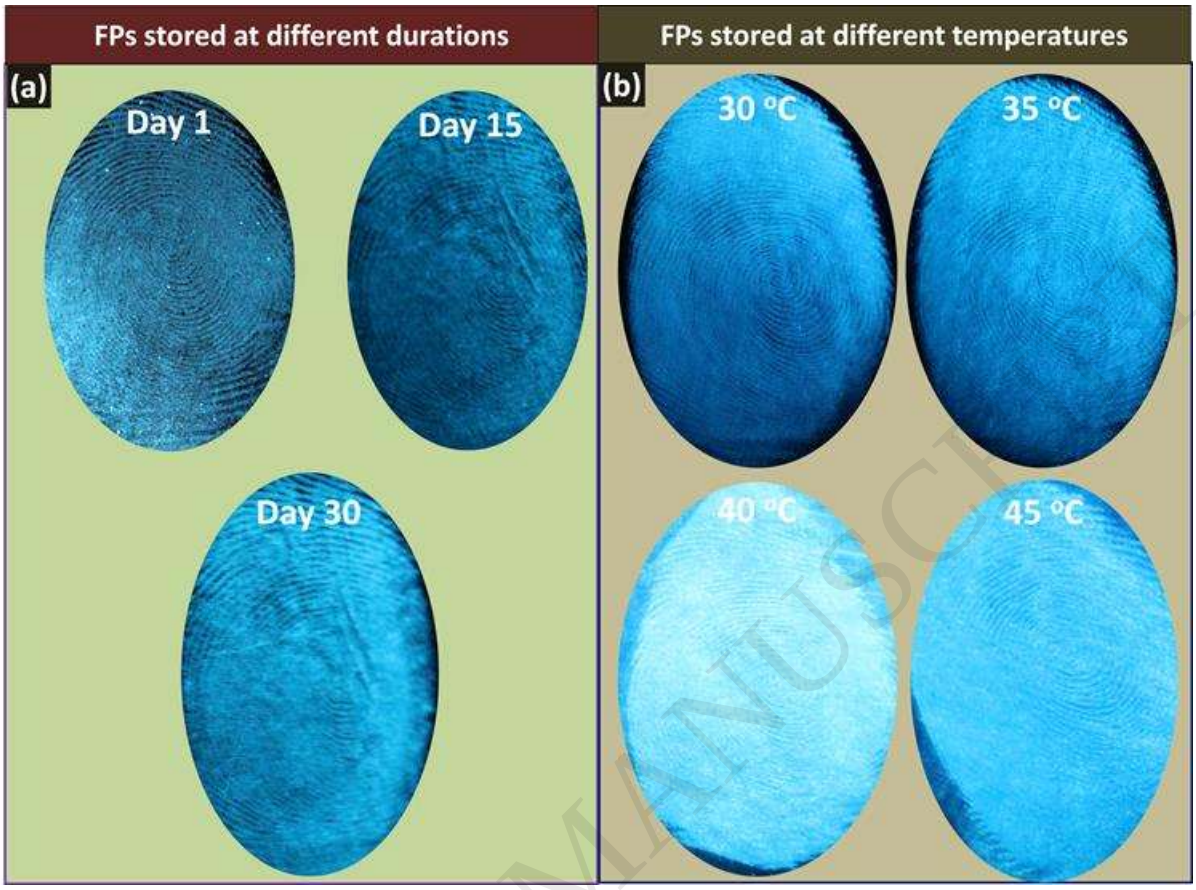

Fig.11 (a) FPs stored at different temperatures and (b) aging of FPs on aluminum foil surface for different durations.

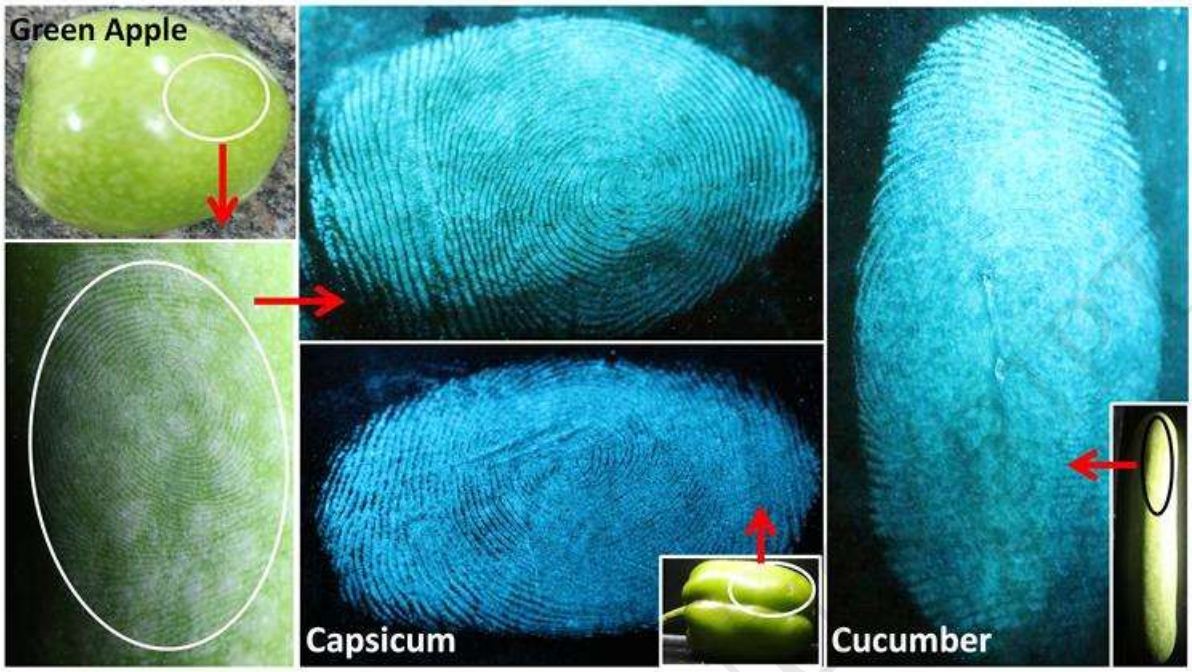

Fig.12. LFPs developed on the surface of green apple, capsicum and cucumber using $BaTiO_3:Nd^{3+}$ (7 mol %) NSs under 254 nm UV light.

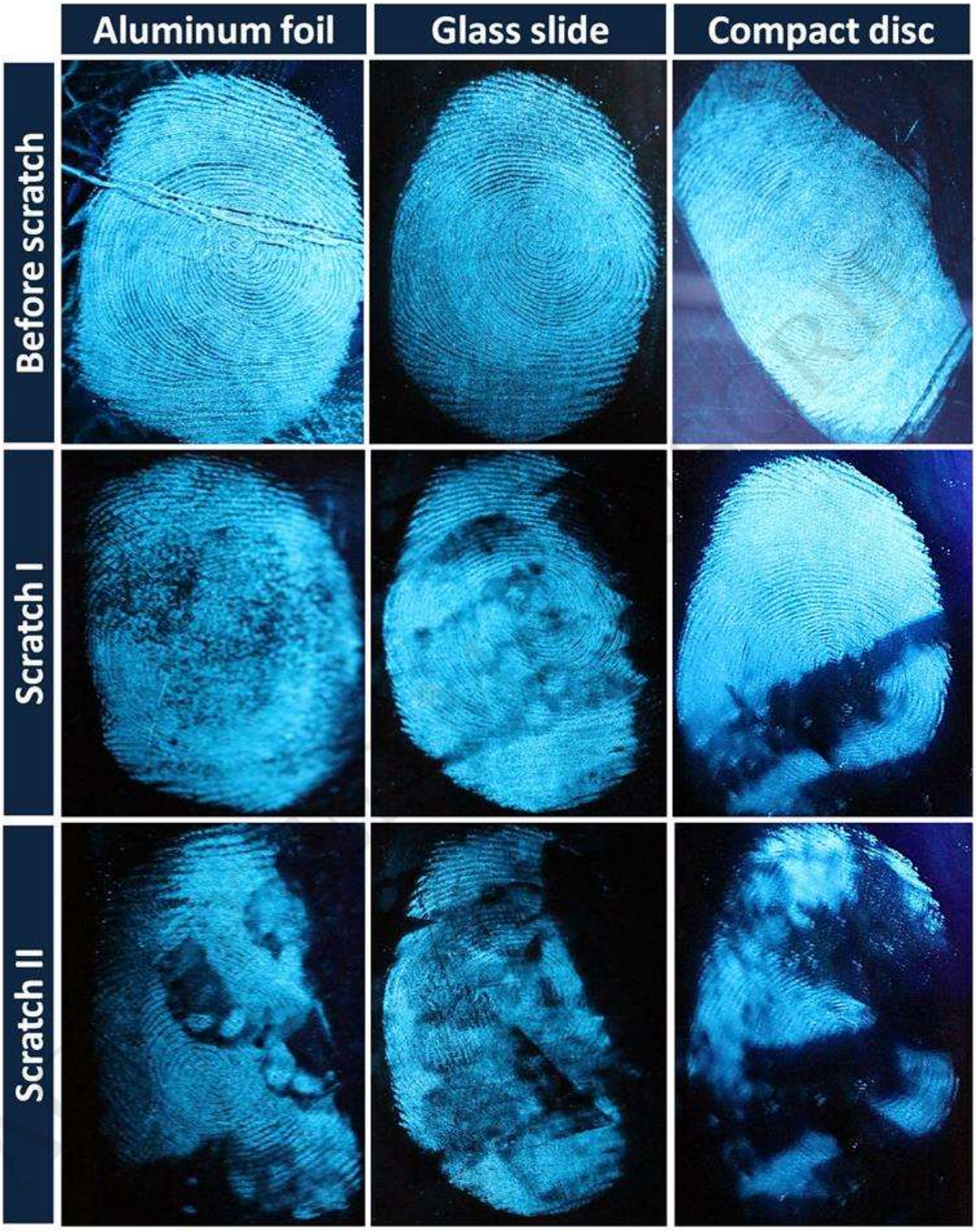

Fig.13 FPs abrasion test on various surfaces.

Table captions:

Table 1: Estimated crystallite size and strain values of $BaTiO_3:Nd^{3+}$ (1-11 mol %) NPs.

Table.2: J-O intensity parameters (Ω_2, Ω_4), Emission peak wavelengths ($\lambda_p$in nm), radiative transition probability (A_T), calculated radiative life time(τ_{rad}) and branching ratio (β_R) of BaTiO3: Nd^{3+} NPs (λ_{ex} = 395 nm).

Table 3: The values of CIE (x, y) coordinates and CCT (K) of $BaTiO_3$: Nd^{3+} (1-11mol %) NPs.

Table 1: Estimated crystallite size and strain values of $BaTiO_3:Nd^{3+}$ (1-11 mol %) NPs.

$BaTiO_3:Nd^{3+}$ (mol %)	**Crystallite size(nm)**		**Strain (x 10^{-4})**	**Energy gap (E_g) eV**
	[Scherrer's approach]	**[W-H approach]**		
1	25	21	1.3	3.29
3	27	24	1.5	3.32
5	29	23	1.7	3.34
7	32	29	1.9	3.36
9	34	31	2.1	3.39
11	36	33	2.3	3.42

Table.2: J-O intensity parameters (Ω_2, Ω_4), Emission peak wavelengths ($\lambda_p$in nm), radiative transition probability (A_T), calculated radiative life time (τ_{rad}) and branching ratio (β_R) of $BaTiO_3$: Nd^{3+} (1-11 mol %) NPs (λ_{ex} = 395 nm).

Nd^{3+} conc. (mol %)	J-O intensity parameters ($\times10^{-20}$ cm^2)		Emission peak wavelength λ_p (nm)	A_T (s^{-1})	τ_{rad} (ms)	β_R	A_{21}
	Ω_2	Ω_4					
1	2.53	5.05	542	52.18	19.16	0.99	1.601
3	3.35	7.68	542	59.46	16.81	0.99	1.102
5	3.14	6.78	541	56.89	17.57	0.99	1.276
7	3.12	6.74	542	56.42	17.72	0.99	1.334
9	3.29	8.12	541	61.35	16.29	0.99	1.582
11	3.42	8.14	542	63.43	15.76	0.99	1.141

Table 3: The values of CIE (x, y) co-ordinates and CCT (K) values of $BaTiO_3$: Nd^{3+} (1-11mol %) NPs.

Nd^{3+} Concentration (mol %)	X	Y	CCT (K)
1	0.2520	0.3349	10283
3	0.2522	0.3357	10239
5	0.2509	0.3324	10466
7	0.2523	0.3360	10211
9	0.2513	0.3333	10400
11	0.2371	0.2973	10320